

2017

## Design and Investigation of de Vries Liquid Crystals Based on 5-Phenyl-Pyrimidine and (R,R)-2,3-Epoxyhexoxy backbone.

S.P. Sreenilayam<sup>\*</sup>

*Trinity College Dublin, Ireland*

D. Rodriguez-Lojo

*Queens University, Belfast*

V. P. Panov

*Trinity College Dublin, Ireland*

*See next page for additional authors*

Follow this and additional works at: <https://arrow.tudublin.ie/engscheleart2>



Part of the [Electrical and Electronics Commons](#)

### Recommended Citation

Sreenilayam, S.P., Rodriguez-Lojo, D. & Panov, V.P. (2017). Design and Investigation of de Vries Liquid Crystals Based on 5-Phenyl-Pyrimidine and (R,R)-2,3-Epoxyhexoxy backbone. *Physical Review*, vol. 96, no. 4. doi:10.1103/PhysRevE.96.042701

*This Article is brought to you for free and open access by the School of Electrical and Electronic Engineering at ARROW@TU Dublin. It has been accepted for inclusion in Articles by an authorized administrator of ARROW@TU Dublin. For more information, please contact [arrow.admin@tudublin.ie](mailto:arrow.admin@tudublin.ie), [aisling.coyne@tudublin.ie](mailto:aisling.coyne@tudublin.ie).*



*This work is licensed under a [Creative Commons Attribution-NonCommercial-Share Alike 4.0 License](#)*

---

**Authors**

*S.P. Sreenilayam", D. Rodriguez-Lojo, V. P. Panov, V. Swaminathan, J. K. Vij, Yuri Panarin, E. Gorecka, A. Panov, and P.J. Stevenson*



# CHORUS

This is the accepted manuscript made available via CHORUS. The article has been published as:

## Design and investigation of de Vries liquid crystals based on 5-phenyl-pyrimidine and (R,R)-2,3-epoxyhexoxy backbone

S. P. Sreenilayam, D. Rodriguez-Lojo, V. P. Panov, V. Swaminathan, J. K. Vij, Yu. P. Panarin, E. Gorecka, A. Panov, and P. J. Stevenson

Phys. Rev. E **96**, 042701 — Published 3 October 2017

DOI: [10.1103/PhysRevE.96.042701](https://doi.org/10.1103/PhysRevE.96.042701)

1 The design and investigation of de Vries liquid crystals based on 5-  
2 phenyl-pyrimidine and (R,R)-2,3-epoxyhexoxy backbone

3 S. P. Sreenilayam,<sup>1</sup> D. Rodriguez-Lojo,<sup>2</sup> V. P. Panov,<sup>1</sup> V. Swaminathan,<sup>1</sup> J. K. Vij,<sup>1\*</sup> Y. P.  
4 Panarin<sup>1,3</sup> E. Gorecka,<sup>4</sup> A. Panov,<sup>2</sup> P. J. Stevenson<sup>2</sup>

5 <sup>1</sup>Department of Electronic and Electrical Engineering, Trinity College Dublin, The University  
6 of Dublin, Dublin 2, Ireland

7 <sup>2</sup>School of Chemistry and Chemical Engineering, Queens University, Belfast, BT7 1NN,  
8 United Kingdom

9 <sup>3</sup>School of Electrical and Electronic Engineering, Dublin Institute of Technology, Dublin 8,  
10 Ireland

11 <sup>4</sup>Department of Chemistry, Warsaw University, Al. Zwirki i Wigury 101, 02089 Warsaw,  
12 Poland

13

14

15 Calamitic liquid crystals (LCs) based on 5-phenyl-pyrimidine derivatives have been  
16 designed, synthesized and characterized. The 5-phenyl pyrimidine core was functionalized  
17 with chiral (R,R)-2,3-epoxyhexoxy chain on one side and either siloxane or perfluoro  
18 terminated chains on the opposite side. The one involving perfluorinated chain shows SmA\*  
19 phase over a wide temperature range of 82 °C, whereas the siloxane analogue exhibits both  
20 SmA\* and SmC\* phases over broad range of temperatures and a weak first order SmA\* -  
21 SmC\* transition is observed. For the siloxane analogue, the reduction factor for the layer  
22 shrinkage  $R$  (relative to its thickness at the SmA\* - SmC\* transition temperature,  $T_{AC}$ ) is  $\sim$   
23 0.373 and layer shrinkage is 1.7% both at a temperature of 13 °C below the  $T_{AC}$ . This  
24 compound is considered to be having “de Vries smectic” characteristics with the de Vries  
25 coefficient,  $C_{deVries}$  of  $\sim$  0.86 on the scale of zero (the maximum layer shrinkage) to 1 (zero  
26 layer shrinkage). A three-parameter mean-field model is introduced for the orientational  
27 distribution function (ODF) to reproduce the electro-optic properties. This model explains the  
28 experimental results and leads to the ODF which exhibits a cross-over from the sugar-loaf to  
29 diffuse-cone ODF some 3 °C below  $T_{AC}$ .

30 Email: [jvij@tcd.ie](mailto:jvij@tcd.ie)

31

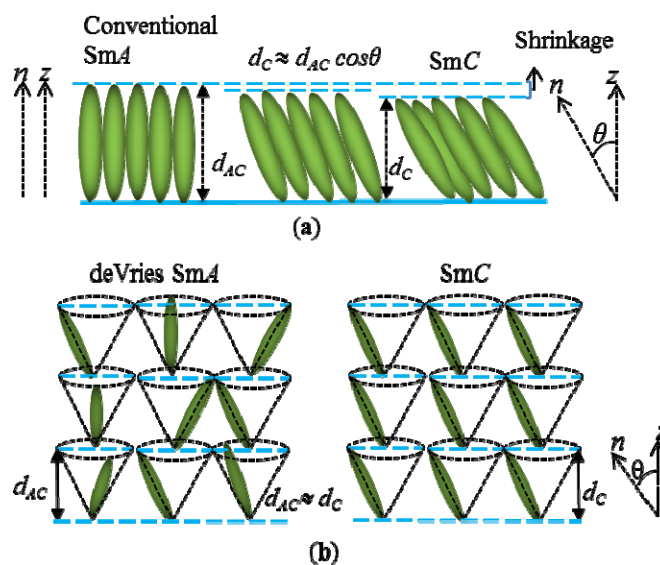
32

## 34 I. INTRODUCTION

35 Chiral smectic liquid crystals (LCs) having mesophases close to the room temperature  
36 are extremely useful for the next generation of displays and electro-optical devices. The  
37 devices based on ferroelectric smectics with extremely fast switching time ( $\mu\text{s}$ ) compared to  
38 the currently used slowly switching nematics (ms) are very promising [1]. However to obtain  
39 the defect free alignment in an LC cell over a broad range of temperatures, a pre-requisite of  
40 zero or a small layer shrinkage for practical applications is required and the achievement of  
41 which is still an open challenge. In principle, one is able to align the material very well in the  
42 nematic or smectic  $A$  phases. However on a phase transition from  $\text{Sm}A$  to  $\text{Sm}C$ , a tilt emerges  
43 whereby the molecular long axis  $\mathbf{n}$  tilts relative to the layer normal  $\mathbf{z}$  by an angle,  $\theta$ , that varies  
44 with temperature (Fig. 1a). Consequently, the layer spacing ( $d_C$ ) in the  $\text{Sm}C$  phase decreases  
45 by a factor of  $\cos\theta$  provided liquid crystalline molecules are close enough to being considered  
46 as rigid rods. The layer shrinkage arising from the tilt together with surface anchoring of  
47 molecules leads to chevron structure/s formed in the cell. These structures with opposite fold  
48 directions create zigzag defects at the interface in between the two oppositely folded  
49 cheverons. The emergence of these defects are impediments to a successful  
50 commercialization of devices based on ferroelectric LCs [2-4]. The solution is therefore  
51 focussed on to developing chiral LCs with a minimal or zero layer-shrinkage at the  $\text{Sm}A^*$ -  
52  $\text{Sm}C^*$  transition temperature and within the temperature range of  $\text{Sm}C^*$  [4]. It is normally  
53 the case that where the layer shrinkage is much lower than the scaling factor,  $\cos\theta$ , then the  
54 smectic phases of such compounds are known as ‘de Vries smectics’ (Fig. 1b).

55 A dozen or so compounds have been identified to have de Vries characteristics to the  
56 varying degrees of perfection. According to the semi-qualitative studies carried out so far, the  
57 calamitic LCs that combine low orientational order parameter but large lamellar orderings  
58 are likely to exhibit better de Vries type characteristics [5-9]. Most of the de Vries smectics  
59 contain trisiloxane/carbosilane backbones and perfluorinated side chains on either ends of the  
60 core; these terminations strongly promote lamellar orderings [10]. In this case, the alkane  
61 chains were replaced by an epoxy group (a precursor in the synthesis of the difluoro  
62 material). In order to obtain a large  $P_S$  in the  $\text{Sm}C^*$  phase, it is pertinent to prepare highly  
63 enantiomeric enriched chiral molecules to avoid the cancelation effects of the oppositely

64 handed enantiomers. In the literature, excellent protocols are given for preparing epoxides  
 65 from allylic alcohols with large enantiomeric excesses [11]. However to our knowledge,  
 66 materials with enantiomeric enriched 5-phenyl pyrimidine epoxides have not yet been  
 67 reported to have de Vries like behavior [12] before. The epoxide group may induce large  
 68 electrical polarization. A use of 5-phenyl pyrimidine though as an aromatic core is  
 69 extensively used in the synthesis of compounds that exhibit de Vries-like characteristics in  
 70 chiral and non-chiral mesogens [13-15]. With this concept in mind, two new chiral materials  
 71 containing epoxides in their structures have been designed, synthesized and investigated.



72

73 **FIG. 1** Schematic representation of the molecular arrangements in the SmA and SmC  
 74 mesophases as per (a) conventional rigid-rod model and, (b) de Vries diffuse cone  
 75 model [16].  $z$  is the layer normal,  $n$  is the molecular long axis orientation,  $\theta$  is the angle  
 76 between  $n$  and  $z$ ,  $d_C$  and  $d_A$  are the layer spacing in SmC and SmA, respectively.

77 In this article, we report synthesis and properties of the two 5-phenyl pyrimidine  
 78 derivatives that contain the chiral (*R,R*)-2,3-epoxyhexoxy chain in conjunction with  
 79 trisiloxane (adpc042) or perfluorinated (DR257) terminal chains (see appendix for the  
 80 synthetic procedure). Both moieties are therefore structurally related to each other, both use  
 81 the same aromatic core and the epoxide chiral chain. In the DR257, siloxane group is  
 82 replaced with perfluorinated butane as aliphatic linkage of six carbons with the aromatic core.  
 83 A modification of the chain ending could have a significant effect on the properties and with  
 84 the objective of finding its effect on the electro-optic properties, we decided to explore this  
 85 further to establish a well-desired structure-property relationship. The mesophases formed by  
 86 these compounds were characterized by differential scanning calorimetry (DSC), polarized

87 optical microscopy (POM), x-ray diffraction (XRD), electro-optics and dielectric  
88 spectroscopy. Characterization of the LCs shows that the perfluorinated epoxide DR257  
89 exhibits a stable SmA\* phase over a broad range of temperatures whereas the siloxane  
90 terminated analogue adpc042 exhibits both SmA\* and SmC\* phases. In this trisiloxane  
91 compound we achieve a layer shrinkage of 1.7 %, at a temperature of -13 °C below the SmA\*  
92 - SmC\* transition temperature. Since adpc042 LC exhibits both SmA\* and SmC\* phases,  
93 properties of this compound are detailed below.

## 94 **II. EXPERIMENT**

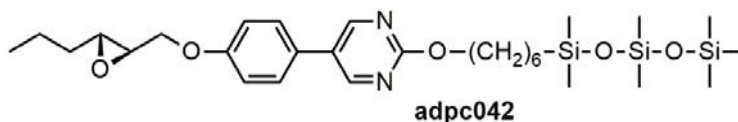
95 The phase sequence and the transition temperatures were found by DSC thermograms  
96 (Perkin-Elmer DSC-7 calorimeter). The experiment was carried out under cooling at a rate of  
97 10 °C min<sup>-1</sup>. The electro-optical studies of the two LCs were conducted using planar-aligned  
98 cells with parallel rubbed polyimide alignment layer KSRP-XX/D611P6NSS05. These cells  
99 were purchased from EHC, Japan. LC cells were studied by POM and electro-optics .  
100 Olympus BX 52, equipped with a rotating table was used. The hot-stage was fixed on to the  
101 rotating table. The hot stage was connected to a temperature controller, Eurotherm 2604.  
102 XRD measurements were carried out on Bruker D8 diffractometer using Cu-K<sub>α</sub> source with a  
103 wavelength 0.154 nm. Dielectric spectroscopic studies were performed using an Alpha High  
104 Resolution Dielectric Analyser (Novocontrol GmbH, Germany) in the frequency range 1 Hz -  
105 10 MHz. Indium Tin Oxide (ITO) coated glass substrates were used to make cells for studies  
106 of the real and imaginary parts of the dielectric permittivity. Substrates were coated with RN  
107 1175 polymer (Nissan Chemicals, Japan) for obtaining the planar alignment. The cell  
108 thickness (*d*) was controlled by Mylar spacers. UV-VIS spectrometer (Avaspec-2048) was  
109 used to measure *d* through interference fringes. The ITO sheet resistance of the substrates (20  
110 Ω/□) is low enough to shift the peak frequency for the resistance of the ITO in series with the  
111 cell, beyond the experimental window of measurements. The dielectric spectra were analysed  
112 using Novocontrol WINDETA program.

## 113 **III. RESULTS AND DISCUSSIONS**

### 114 **A. Differential Scanning Calorimetry and Polarizing Optical Microscopic Studies**

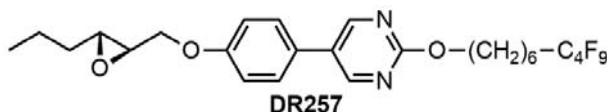
115 The molecular structure and the transition temperatures of siloxane pyrimidine  
116 adpc042 and the fluorinated pyrimidine DR257 are given in Figs. 2 (a) and (b) (synthetic

117 procedures given in the appendix). Result of a DSC thermogram of DR257 is given in Fig.  
 118 2c. Here two transitions with the enthalpies,  $\Delta H$  of  $\sim 17.2 \text{ Jg}^{-1}$  and  $\sim 30.4 \text{ Jg}^{-1}$  at temperatures  
 119 of  $\sim 143 \text{ }^\circ\text{C}$  and  $\sim 56 \text{ }^\circ\text{C}$  are recorded. To identify the mesophases, textures of a  $9 \mu\text{m}$  planar  
 120 cell filled with DR257 are recorded with POM. Images corresponding to the two mesophases  
 121 are shown in the inset of Fig. 2c. On cooling from the isotropic temperature, the mesophase  
 122 grows from the typical ‘batonnet’ structures to the focal conic texture. Both focal conic and  
 123 dark homeotropic textures obtained by POM are the characteristics of  $\text{SmA}^*$  phase [17].  
 124 Textures confirm that the phase transition from  $\text{SmA}^*$  to a crystalline state is at a temperature  
 125 of  $56 \text{ }^\circ\text{C}$ .



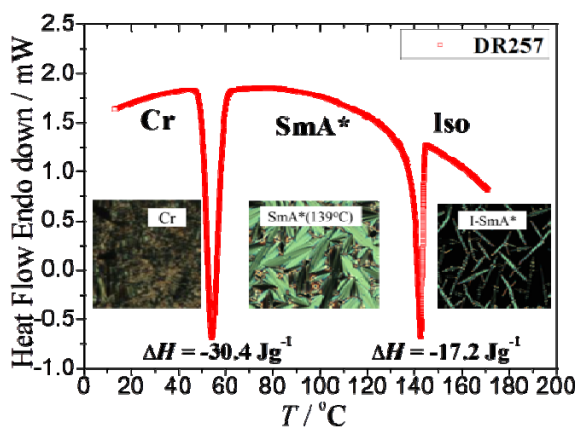
126  
 127 Cr  $-5 \text{ }^\circ\text{C}$   $\text{SmC}^*$   $58 \text{ }^\circ\text{C}$   $\text{SmA}^*$   $82 \text{ }^\circ\text{C}$  Iso

128 (a)

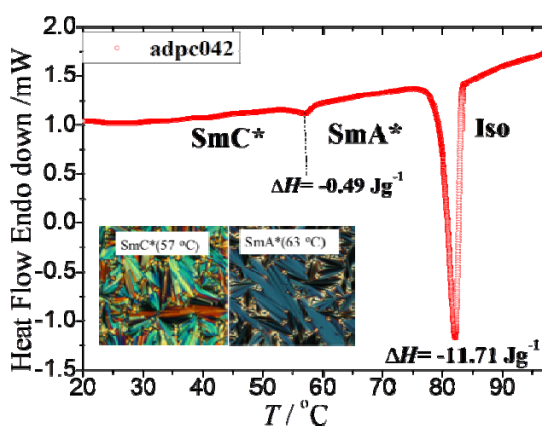


129 Cr  $60 \text{ }^\circ\text{C}$   $\text{SmA}^*$   $152 \text{ }^\circ\text{C}$  Iso

130  
 131 (b)



132 (c)



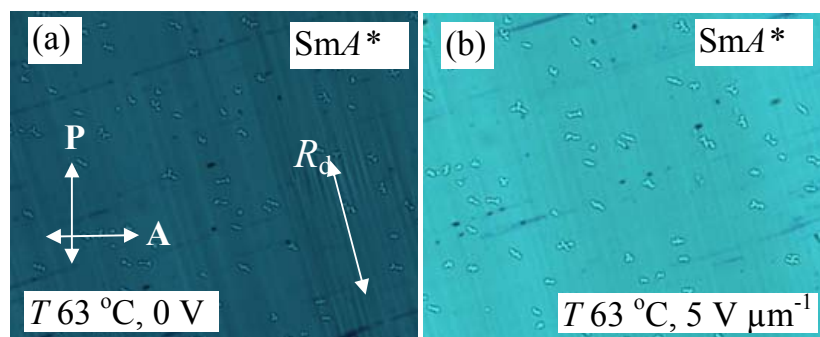
133 (d)

134 **FIG. 2** Molecular structures and the DSC thermograms of adpc042 [(a) and (d)] and  
 135 DR257 [(b) and (c)] are given. The phase transition temperatures are obtained under the  
 136 cooling cycle with a quasi-equilibrium condition at the rate of  $\sim 1 \text{ }^\circ\text{C min}^{-1}$  using POM.  
 137 The cooling curves of the DSC thermograms are obtained at the rate of  $10 \text{ }^\circ\text{C min}^{-1}$ .  
 138 Iso= isotropic phase, Cr= crystalline state. Insets in these two figures are the POM  
 139 images of the mesophases seen under the crossed polarizers. Textures are recorded for a  
 140  $9 \mu\text{m}$  planar-aligned cells in the cooling run.



141 A representative the DSC plot of adpc042 LC under cooling exhibits two peaks (Fig.  
 142 2d). Both DR257 and adpc042 show the first order Iso -SmA\* transition with  $\Delta H$  of  $\sim 11.71$   
 143  $\text{Jg}^{-1}$  and  $17.2 \text{ Jg}^{-1}$  at a temperature of  $\sim 82 \text{ }^\circ\text{C}$  and  $\sim 145 \text{ }^\circ\text{C}$ . This is confirmed by POM where  
 144 the focal conic fan shaped texture from a  $9 \text{ }\mu\text{m}$  planar-aligned cell (Fig. 2d inset) is recorded.  
 145 On lowering the temperature, the sample undergoes a weakly first order SmA\* - SmC\*  
 146 transition with  $\Delta H$  of  $\sim 0.49 \text{ Jg}^{-1}$  ( $0.069 \text{ kcal mol}^{-1}$ ) at  $58 \text{ }^\circ\text{C}$  [12, 18]. For a conventional  
 147 SmA\*- SmC\* transition where the tilt angle stays at almost zero value in the SmA\* phase  
 148 down to the transition temperature  $T_{AC}$ , the DSC thermogram exhibits a second order  
 149 transition with a step in the baseline without a peak for the enthalpy of transition [19]. The  
 150 SmC\* phase of adpc042 is distinguishable from SmA\* by POM where a fan shaped texture  
 151 from a planar cell is altered to a broken fan shaped one (inset Fig. 2d). The dark homeotropic  
 152 texture is changed to Schlieren texture on transition from SmA\* to SmC\*. The entire  
 153 replacement of trisiloxane in adpc042 by tetra fluorocarbon chain in DR257, radically alters  
 154 the mesomorphic behaviour, the temperature range of SmA\* is increased from  $23 \text{ }^\circ\text{C}$  to  $89 \text{ }^\circ\text{C}$ ,  
 155 whereas SmC\* disappears. An increased temperature range of the SmA\* phase in DR257  
 156 could be due to a large dipole moment associated with the fluorinated tail [20]. The siloxane  
 157 groups in adpc042 enhance the thermal stability of the compound as well as lower the phase  
 158 transition temperatures. These features may be of great importance from a point of view of  
 159 the molecular design and applications.

160 The POM images of a planar-aligned cell of thickness  $9 \text{ }\mu\text{m}$  filled with adpc042  
 161 recorded at  $63 \text{ }^\circ\text{C}$  ( $\sim 19 \text{ }^\circ\text{C}$  below the Iso- SmA\* transition temperature and  $5 \text{ }^\circ\text{C}$  above the  
 162  $T_{AC}$ ), are given in Fig. 3. The rubbing direction  $R_d$  is fixed at an angle,  $\alpha = \sim 15^\circ$  to the  
 163 polarizer  $\mathbf{P}$ .



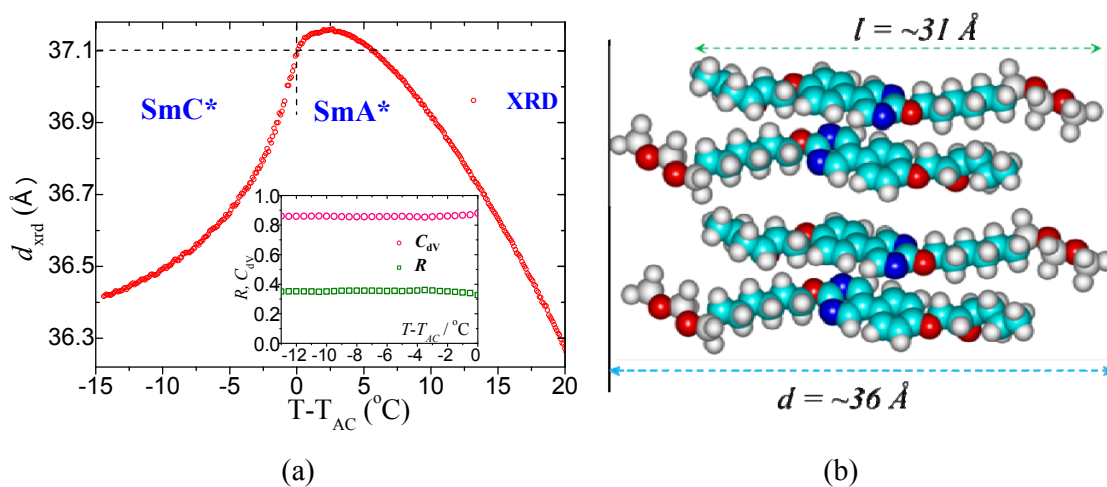
164  
 165  
 166  
 167

**FIG. 3** POM images of SmA\* phase at a temperature of  $63 \text{ }^\circ\text{C}$  in a  $9 \text{ }\mu\text{m}$  planar-aligned cell filled with adpc042 LC: (a)  $0 \text{ V}$  and (b)  $5 \text{ V } \mu\text{m}^{-1}$  (square wave AC electric field of  $110 \text{ Hz}$ ).

168 The electric field treatment of the LC cell gives rise to a uniform mono-domain  
 169 texture (Fig. 3). An application of the external electric field across a cell in well-aligned  
 170 SmA\* phase produces a change in the color of the texture (compare Figs. 3a and 3b), due to  
 171 an increase in the birefringence  $\Delta n$  with the field, a characteristic of the de Vries behavior. In  
 172 this phase, the molecules are tilted but are azimuthally disordered. The electric field produces  
 173 a bias in the azimuthal distribution and the molecules tilt in a particular direction determined  
 174 by the polarity of the field. The resulting SmA\* is reduced to the same symmetry as SmC\*  
 175 phase through azimuthal ordering of the already tilted liquid crystalline molecules.

## 176 B. X-ray diffraction(XRD)

177 Figure 4(a) shows the temperature dependence of the smectic layer spacing  
 178 determined by the XRD experiment. On cooling the sample below the isotropic phase, the  
 179 layer spacing in SmA\* phase initially increases linearly with decreasing temperature. On  
 180 approaching the SmA\*- SmC\* transition temperature, the thickness reverses its trend within  
 181 SmA\* from an increase to a decrease due to an emergence of the molecular tilt even in the  
 182 SmA\* phase. On further cooling of the sample cell, the layer thickness in the SmC\* phase  
 183 continues to decrease much more slowly than expected from a conventional smectic, in  
 184 which the layer thickness scales as,  $\cos \theta$ . Figure 4b shows the simulated molecular  
 185 structures of the compound adpc042 using Hyperchem Program. The simulated length  $l$ , of  
 186 the molecule is  $\sim 31 \text{ \AA}$ . A possible molecular arrangement in layers is shown in Fig. 4b such  
 187 that the total length of a pair of molecules is larger than the smectic layer thickness.



188  
 189  
 190 **FIG. 4** (a) Temperature dependence of the smectic layer spacing determined by XRD ( $\blacktriangle$ )  
 191 relative to the layer thickness at the SmA\* to SmC\* transition temperature. The inset  
 192 shows plots of the de Vries coefficient  $C_{\text{deVries}}$  ( $\square$ ) and the reduction factor  $R$  ( $\square$ ) vs. the

193 reduced temperature ( $T-T_{AC}$ ). De Vries characteristics are defined in terms of  $C_{deVries}$  and  
 194  $R$ . Measurements are carried out on a compound adpc042, (b) The simulated molecular  
 195 structures of the compound adpc042.

196 A layer shrinkage of 1.7% is calculated from the XRD at a temperature of 13 °C below the  
 197  $SmA^*$ -  $SmC^*$  transition temperature  $T_{AC}$ . The layer-shrinkage is small. The behaviour is  
 198 similar to that in  $SmA^*$  phase where the molecular directors in  $SmA^*$  phase are distributed  
 199 on to a cone where the azimuthal angle is degenerated. At the  $SmA^*$  to  $SmC^*$  transition,  
 200 the tilt directions condense to within narrower limits, hence the disorder in the azimuthal  
 201 angle disappears in the  $SmC^*$  phase. This process in itself requires no change in the layer  
 202 thickness.

203 The reduction factor  $R$  of a smectic LC is defined as,

$$204 \quad R = \frac{\delta(T)}{\theta_{opt}(T=T_{AC})} = \frac{\cos^{-1}(d_c(T)/d_{AC}(T=T_{AC}))}{\theta_{opt}(T=T_{AC})} \quad (1)$$

205 where  $\delta(T)$  governs the layer thickness at a temperature  $T$  within  $SmC^*$  phase relative to the  
 206 layer thickness at the  $SmA^*$ -  $SmC^*$  transition temperature,  $d_{AC}$ , on assuming that the rigid  
 207 rod model is applicable to the LC under investigation [21].  $\theta_{opt}$  is the optical tilt angle  
 208 determined by the POM (Fig. 5). According to Eq. (1), an ideal de Vries smectic with  
 209  $d_c(T) \approx d_{AC}(T = T_{AC})$  (Fig. 1b) produces a defect-free bookshelf geometry in  $SmC^*$   
 210 phase with a reduction factor  $R = 0$ , *i.e.* the short-range molecular tilt order at a lower  
 211 temperature in the  $SmA^*$  phase becomes long range close to the  $SmA^*$ -  $SmC^*$  transition  
 212 temperature, where the maximum de Vries cone angle is equal to the saturated optical tilt  
 213 angle at a temperature close to  $T_{AC}$ . On entering the  $SmC^*$  from  $SmA^*$  phase, the azimuthal  
 214 ordering of the molecular directors on the cone localizes these on to a single orientation. In  
 215 this case, the layer contraction is absent and then  $d_c/d_{AC} \approx 1$ , and therefore  $R \approx 0$ . Li *et al.*  
 216 suggested another method of characterizing de Vriesness from measurements of the layer  
 217 thickness from XRD in terms of the de Vries co-efficient,  $C_{deVries}$  [22]. The magnitude of this  
 218 varies from '0' (classic rigid rod model with a maximum layer shrinkage) to 1 (ideal de Vries  
 219  $SmA^*$  –  $SmC^*$  transition with zero layer shrinkage) such that

$$C_{deVries} = 1 - \left[ \frac{(d_{AC} - d_C)}{(d_{AC}(1 - \cos \theta))} \right] \quad (2)$$

220 The material adpc042 gives rise to  $R \approx 0.373$  at 13 °C below the SmA\* - SmC\* transition  
 221 temperature. Understandably,  $R$  is away from zero but still low, hence the material is close to  
 222 being a ‘de Vries smectic’. An estimated value of  $C_{deVries}$  is  $\sim 0.86$  (Fig. 3 inset) at 13 °C  
 223 below the SmA\* - SmC\* transition temperature. The inset plot of Fig. 4 shows that both  $R$   
 224 and  $C_{deVries}$  are almost independent of temperature throughout the entire temperature range of  
 225 the SmC\* phase. The lowest reported value of  $R$  so far is 0.17 for the chiral de Vries  
 226 compound **QL32-6** that exhibits a maximum layer contraction of only 0.2% at 3 °C below the  
 227 SmA\*-SmC\* transitions with an optical tilt angle of 20° [13].  
 228

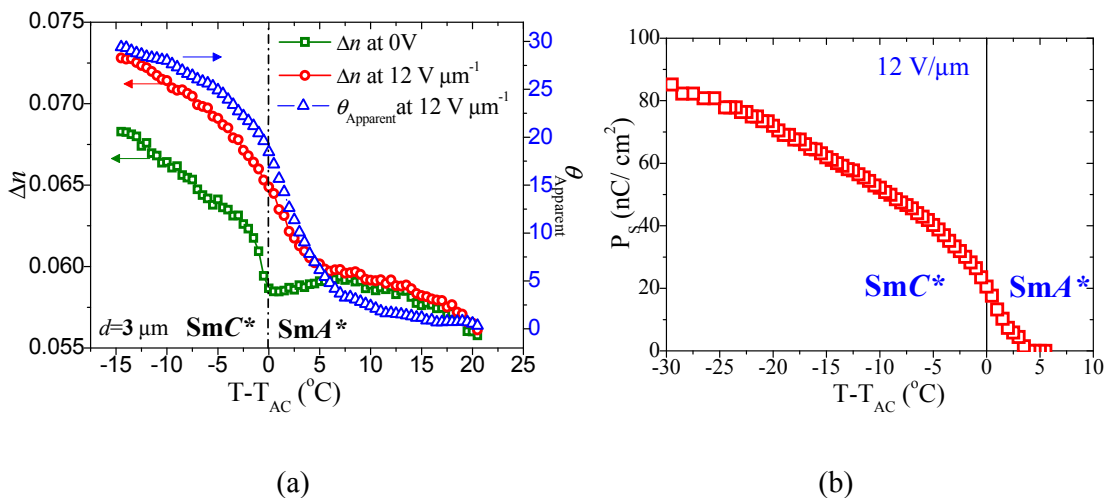
### 229 C. Electro-optical studies

230 The birefringence  $\Delta n$  and the apparent optical tilt angle  $\theta_{Apparent}$  are determined by  
 231 recording the intensity of a transmitted beam of light through a LC cell by varying the  
 232 positions of the polarizer and the analyzer. The procedure involves first keeping **P** fixed, and  
 233 then rotating the analyzer automatically by various angles. This procedure is repeated for at  
 234 least three different positions of the polarizer. From the data,  $\Delta n$  and  $\theta_{Apparent}$  are  
 235 calculated. This procedure is different from that given by Park *et al.* [23], who record the  
 236 transmitted intensity by rotating the sample and also record the transmitted intensity for the  
 237 P and A (i) parallel and (ii) crossed to each other. The experiment is conducted by applying a  
 238 triangular signal of frequency 46 Hz and an amplitude of 12 V<sub>0-peak</sub>  $\mu\text{m}^{-1}$ . Frequency of the  
 239 field is chosen so as to allow sufficient time for the electro-optic switching to occur but to  
 240 prevent ionic-conductivity contributing to the switching current. An amplitude of the voltage  
 241 applied to the LC sample adpc042 is large enough so as to make the tilt angle increase slowly  
 242 with field and then eventually to saturate by the field while avoiding a risk of damage to the  
 243 sample by the applied electric field.

244 Figure 5 shows results of the birefringence ( $\Delta n$ ) as a function of temperature with and  
 245 without electric field applied across the cell. On cooling the sample in the absence of field  
 246 from the isotropic to SmA\* phase, the magnitude of  $\Delta n$  first increases slightly, but then starts  
 247 to decrease within SmA\* phase. This decrease in  $\Delta n$  with temperature is due to the de Vries  
 248 tilt appearing in the SmA\* phase and a distribution of the in-layer directors occurring on to  
 249 the cone. On further cooling the sample in the absence of electric field,  $\Delta n$  suddenly increases

250 at the  $\text{SmA}^* - \text{SmC}^*$  phase transition temperature  $T_{AC}$  followed by slow increase with a  
 251 decrease in temperature. An application of the electric field ( $E=12 \text{ V } \mu\text{m}^{-1}$ ) gives rise to a  
 252 continuous rise in  $\Delta n$  in the entire temperature range of the  $\text{SmA}^*$  and  $\text{SmC}^*$  phases. This  
 253 field induced increase in  $\Delta n$  is consistent with a change in the interference colors observed by  
 254 POM (Fig. 3). The behavior is typical of the diffuse-cone model of  $\text{SmA}^*$  phase with a weak  
 255 first order  $\text{SmA}^* - \text{SmC}^*$  phase transition (Fig. 2b). In the conventional  $\text{SmA}^*$  of a LC, one  
 256 may expect a small increase in  $\Delta n$  to occur at the phase transition from a uniaxial  $\text{SmA}^*$  (with  
 257 zero tilt angle at  $T = T_{AC}$ ) to a biaxial  $\text{SmC}^*$  phase.

258 For adpc042, the measured value of the spontaneous polarization  $P_S$  [24] is plotted as  
 259 a function of the reduced temperature in Fig. 5(b). Measurements are carried out on a  $5 \mu\text{m}$   
 260 planar cell under the application of a square wave, frequency 110 Hz and large enough  
 261 amplitude of  $12 \text{ V}/\mu\text{m}$ . The field is such that the helical structure for temperatures within  
 262  $\text{SmC}^*$  is unwound. It is interesting to note that the field induced polarization is much higher  
 263 than for conventional ferroelectric liquid crystals.  $P_S$  increases with a reduction in  
 264 temperature below the  $\text{SmC}^* - \text{SmA}^*$  transition. The liquid crystalline material under study  
 265 yields  $P_S \sim 82.5 \text{ nC cm}^{-2}$  for  $T=(T_{AC} - 30)^\circ\text{C}$ .

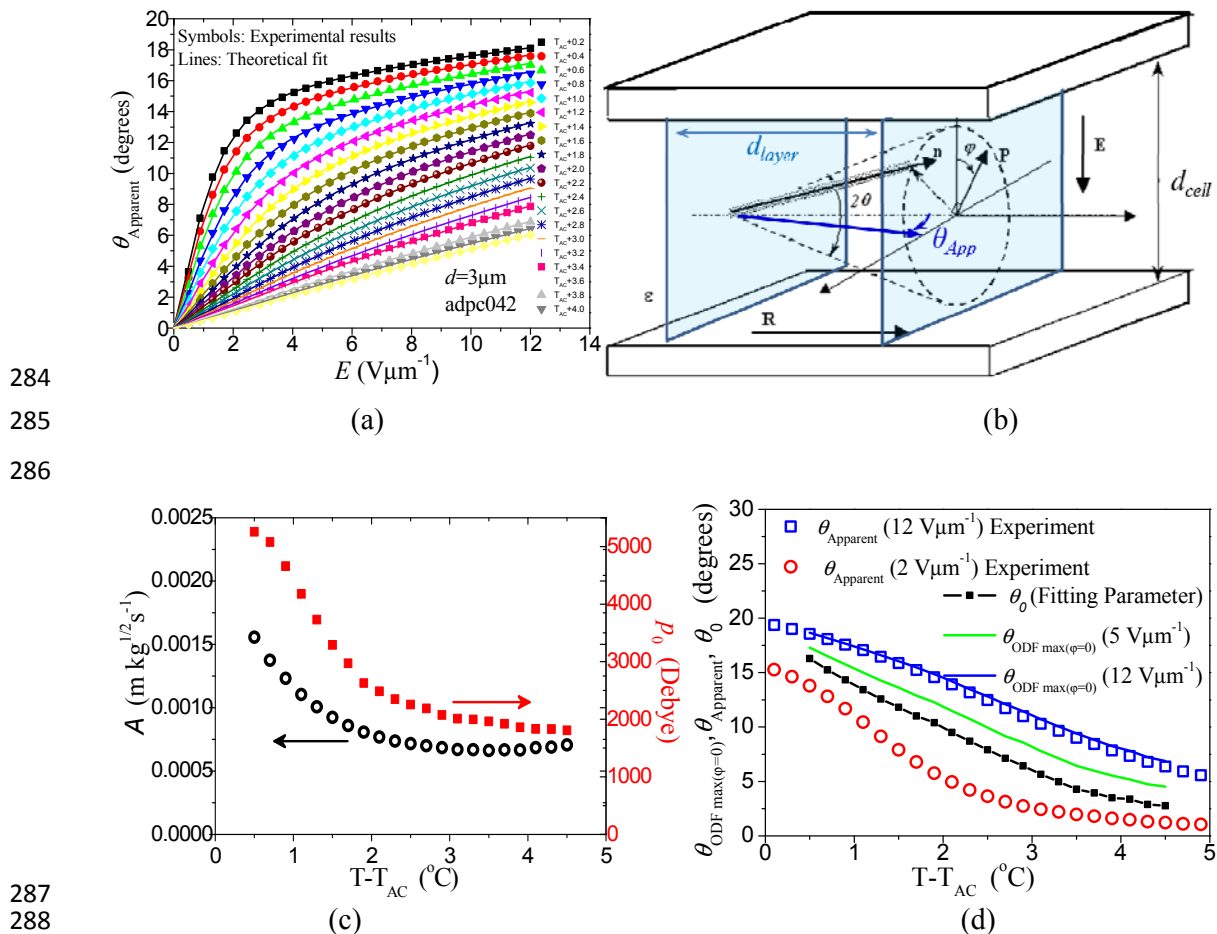


266

267

268 **FIG. 5.** Results given here are for adpc042. (a) The temperature dependence of  
 269 the apparent tilt angle ( $\theta_{\text{Apparent}}$ ) and the birefringence  $\Delta n$  by applying a maximum  
 270 field of ( $12 \text{ V } \mu\text{m}^{-1}$ , red open circles);  $\Delta n$  in the absence of the electric field  
 271 (green square). Blue triangles denote the apparent tilt angle  $\theta_{\text{Apparent}}$  for a field of  
 272  $12 \text{ V}/\mu\text{m}$ . Measurements are carried out on a  $3 \mu\text{m}$  planar-aligned cell filled with  
 273 adpc042 LC. (b) Spontaneous polarization  $P_S$  measured under the cooling process  
 274 from the isotropic temperature plotted as a function of  $(T - T_{AC})$ . The  
 275 measurements are carried out on a  $5 \mu\text{m}$  planar cell by applying a square wave AC  
 276 voltage of  $12 [V_{\text{peak-peak}}/\mu\text{m}]$  at a frequency of 110 Hz.

277 The measured values of  $\theta_{\text{Apparent}}$  as a function of the electric field for different  
 278 temperatures in the  $\text{SmA}^*$  phase are plotted in Fig. 6a. The co-ordinate system and the  
 279 definition of the various angles are given in Fig. 6b. At a higher temperatures in the  $\text{SmA}^*$   
 280 phase, the magnitude of  $\theta_{\text{Apparent}}$  is low and it increases linearly with the applied field. For  
 281 temperatures closer to the  $T_{\text{AC}}$ ,  $\theta_{\text{Apparent}}$  becomes nonlinear and it continues to increase slowly  
 282 up to an electric field of  $12 \text{ V } \mu\text{m}^{-1}$  and eventually the tilt angle tends to saturate with the  
 283 electric field.



287  
 288  
 289 **FIG. 6.** (a) Variation of the field induced apparent optical tilt  $\theta_{\text{Apparent}}$  (symbols) and  
 290 the corresponding fitted values (solid lines) for selected temperatures. Measurements  
 291 are carried out in a  $3 \mu\text{m}$  planar cell filled with adpc042 LC. (b) The schematic of the  
 292 dynamics with the laboratory co-ordinate system (c) Temperature dependence of the  
 293 model parameters  $A$  and  $p_0$  found from the experiments, (d) temperature dependencies  
 294 of the measured apparent tilt angle  $\theta_{\text{Apparent}}$  (open symbols), the cone angle  $\theta_0$  (the line  
 295 with symbols) positions of the distribution function of the maxima (lines) for the  
 296 various electric field strengths applied across a planar-aligned cell.

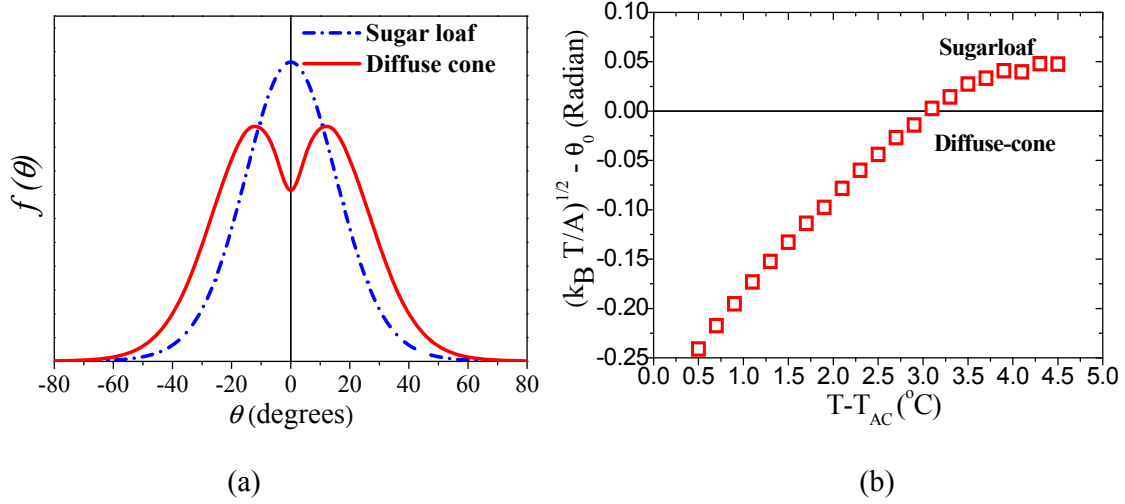
297 Several approaches exist in the literature for modeling the unusual electro-optic  
 298 characteristics of the de Vries smectics [25-30]. The Langevin-Debye model, proposed by

299 Fukuda [25] in a different context, was used by Clark *et al.* [27] to explain the electro-optical  
 300 properties of de Vries smectic LCs. This model assumes that for a fixed temperature and zero  
 301 electric field, the molecular directors in the SmA\* phase are tilted but azimuthally distributed  
 302 on to a cone. In this model, the free energy is expressed as  $U = -pE \cos \varphi$ , where  $p$  is the local  
 303 dipole moment. However, this model does not correctly explain the dependence of the  
 304 induced apparent tilt angle ( $\theta_{\text{Apparent}}$  for the electric field) for temperatures rather closer to the  
 305 SmA\*-SmC\* transition temperature  $T_{\text{AC}}$ . In 2013, the Boulder group [28] modified this  
 306 model where they added an additional term involving the square of the electric field in the  
 307 expression for the free energy. This is expressed as  $U = -p_0 E \sin \theta \cos \varphi (1 + \alpha E \cos \varphi)$ .  
 308 Here,  $\alpha$  is the phenomenological scaling factor and  $p_0 \sin \theta$  is the dipole moment of the  
 309 domain correlated in the molecular tilt created by the condensation of azimuthal angles  $\varphi$ .  
 310 The first term  $-p_0 E \sin \theta \cos \varphi$  corresponds to the interaction of the dipole with the field.  
 311 The second term  $-\alpha p_0 E^2 \sin \theta \cos^2 \varphi$  includes the tilt susceptibility that increases with the  
 312 square of the field  $E$  and it leads to a sigmoidal response in both  $\Delta n$  and  $\theta_{\text{Apparent}}$  with  $E$ . In  
 313 this model, the field induced  $\theta_{\text{Apparent}}$  varies between the values inferred from the  $\Delta n$  at zero  
 314 field ( $\theta_{\text{min}}$ ) to the maximum electric field ( $\theta_{\text{max}}$ ). These limiting values of  $\theta_{\text{min}}$  and  $\theta_{\text{max}}$   
 315 themselves are temperature independent but the actual values within these limits nevertheless  
 316 are temperature dependent. Therefore, we propose a somewhat different model. This  
 317 involves three parameters for explaining the electro-optic response where the mean-field free  
 318 energy is expressed as:

$$319 \quad U = -p_0 E \sin \theta \cos \varphi + A^2 \sin^2(\theta - \theta_0) \quad (3)$$

320 Here the first term,  $p_0 E \sin \theta \cos \varphi = \mathbf{P} \cdot \mathbf{E}$ , describes the usual dipole interaction energy  
 321 with the field.  $|\mathbf{P}|, [= (p_0 \sin \theta)]$ , is the magnitude of the dipole moment of a tilt correlated  
 322 domain. **This first term of Eq. (3) is linear in the external electric field  $E$ .** The second term in  
 323 this equation defines the cone distribution with a cone aperture angle of  $2\theta_0$  and a distribution  
 324 width proportional to  $\sqrt{k_B T}/A$ . Here  $k_B$  is the Boltzmann constant,  $T$  is the absolute  
 325 temperature and  $A$  is the phenomenological co-efficient for the zero field molecular  
 326 distribution. Note that for the case,  $\theta_0 < \sqrt{k_B T}/A$ , the model produces “sugar-loaf” ODF (Fig.  
 327 7(a)), while a larger  $\theta_0$  combined with a narrower distribution width correspond to the  
 328 “volcano” or “diffuse-cone” distribution (Fig. 7(a)). **Thus both scenarios discussed in [31] are**  
 329 **reproduced with the same expression for the free energy.** Figure 7b illustrates the trend of  
 330  $[(k_B T/A)^{1/2} - \theta_0]$ , as a function of the reduced temperature  $(T - T_{\text{AC}})$  for adpc042. One can see

331 that at 2 to 3 degrees below the phase transition, this function crosses zero. This is a cross-  
 332 over between the sugar-loaf and the diffuse-cone ODFs.



333

334

335 **FIG. 7.** (a) 2D schematic representation of sugar-loaf (dash-dot lines in blue colour)  
 336 and diffuse-cone (solid lines in red colour) ODFs. (b)  $[(k_B T/A)^{1/2} - \theta_0]$  plotted as a  
 337 function of the reduced temperature  $(T-T_{AC})$ . Measurements are carried out on a  $3 \mu\text{m}$   
 338 planar cell filled with adpc042.

339 For the range of the electric fields used, we observe no inflection point in the field  
 340 dependence of  $\theta_{\text{Apparent}}$  *i.e.* no change in the slope of the derivative of the angle at the point.  
 341 Therefore, we can achieve a good fit of the experimental data to the model without using  
 342 terms of higher powers of  $E$ .

343 In order to simulate the behaviour of  $\theta_{\text{Apparent}}$ , we use the mean-field approach combined with  
 344 equations for the optical response [28]. An average  $\langle Y \rangle$  over the orientational distribution can  
 345 be written as  $\langle Y \rangle = \int_0^{2\pi} \int_0^{\pi/2} Y(\theta, \varphi) f(\theta, \varphi) \sin \theta d\theta d\varphi$ , where the mean field ODF  $f(\theta, \varphi)$  is  
 346 expressed as:

$$347 \quad f(\theta, \varphi) = \exp[-U/k_B T] / \int_0^{2\pi} \int_0^{\pi/2} \exp[-U/k_B T] \sin \theta d\theta d\varphi \quad (4)$$

348 The apparent electro-optical tilt angle  $\theta_{\text{Apparent}}$  is given by:

$$349 \quad \tan 2\theta_{\text{Apparent}} = \frac{\langle \sin 2\theta \cos \varphi \rangle}{\langle \cos^2 \theta - \sin^2 \theta \cos^2 \varphi \rangle} \quad (5)$$

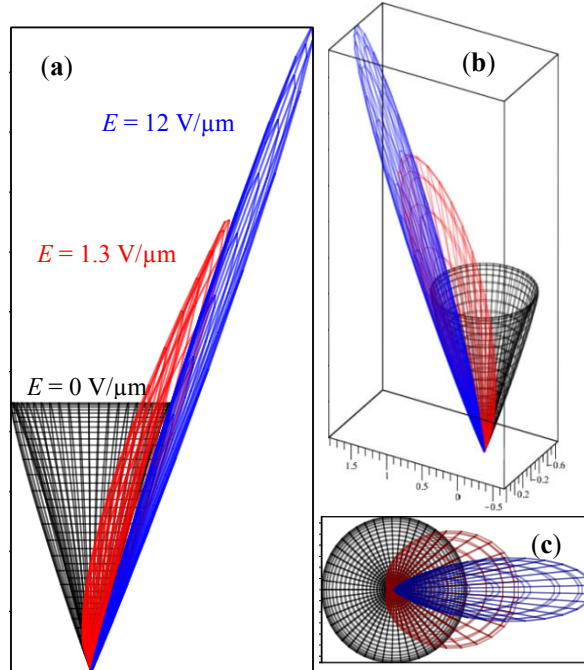
350 On fitting the experimentally obtained voltage dependencies of  $\theta_{\text{Apparent}}$  to the above model,  
 351 we obtain values of  $p_0$ ,  $A$  and  $\theta_0$  each as a function of temperature (Fig. 6c, and 6d). All the  
 352 parameters tend to increase on approaching  $T_{AC}$  as the cell is cooled from the isotropic state  
 353 to the  $\text{SmA}^*$  phase. Such an increase is in agreement with the previous models [27, 28].



354 Onusing the dipole moment of the correlated domain as  $p_0 \approx 5000$  D at  $0.5$  °C above  
 355 the SmC\* - SmA\* phase transition temperature, we can estimate the effective size of a  
 356 domain using the procedure similar to that adopted by Shen et al. [28]. The effective  
 357 molecular dipole moment can be estimated from the polarization density measurements  
 358 performed on a planar-aligned cell in SmC\* phase. In this case  $P_S$  is saturated at  $69$  nC/cm<sup>2</sup>;  
 359  $\theta_{Apparent} = 30^\circ$  at  $(T_{AC} - 19)$  °C, with the molar mass,  $M = 590.3$  g/mol, density  $\rho = 1.2$   
 360 g/cm<sup>3</sup>, the dipole moment is found as  $\mu_{eff} = \frac{P_S M}{\rho N_A \sin \theta_{Apparent}} \approx 0.34$  D. Therefore, the tilt-  
 361 correlated domain in our experiment contains approximately 6, 000 to 15,000 molecules. The  
 362 effective domain correlation length  $\sqrt[3]{\frac{p_0 \sin \theta_{Apparent}}{P_S}}$ , at a temperature close to the SmA\* -  
 363 SmC\* phase transition, is of the order of 30 nm [30].

364 Parameter  $A$  clearly favours the “volcano”- type distribution as illustrated by Fig. 8. A  
 365 comparison of the cone angle  $\theta_0$  that fits the experimentally obtained  $\theta_{Apparent}$  for different  
 366 fields is shown in Fig. 6d. Note that for higher field strengths,  $\theta_{Apparent}$  exceeds  $\theta_0$ . This is  
 367 indicative of a large electro-clinic effect. The solid lines in Fig. 6d show angular positions of  
 368 the maximum in the ODF simulated for the two electric field strengths ( $5$  and  $12$  V $\mu\text{m}^{-1}$ )  
 369 here. The experimental values of  $\theta_{Apparent}$  for  $12$  V $\mu\text{m}^{-1}$  are slightly lower than for an angle for  
 370 which  $\theta_{ODF}$  is a maximum. This is expected from a highly distorted diffuse-cone ODF, the  
 371 distortion is brought about by the applied electric field.

372 Figures 8a-d show a 3D illustration of the ODF function obtained for a temperature of  
 373  $(T_{AC} + 1)$  °C. The ODF is normalized as given below such that its volume for different fields  
 374 is a constant:  $f_{3D} = \frac{f(\theta, \varphi)}{\sqrt[3]{\int_0^{2\pi} \int_0^{\pi/2} f(\theta, \varphi)^3 \sin \theta d\theta d\varphi}}$ . Figure 8c shows the cross-section of the ODF  
 375 in the plane of the LC cell where the maximum of the ODF vs. apparent tilt angle is plotted.  
 376 The electro-clinic effect for the following electric fields are given in Fig. 8: zero, moderate  
 377 ( $1.3$  V/ $\mu\text{m}$ ) (“cone unwinding”), and for large fields;  $12$  V/ $\mu\text{m}$  (tilt increases but  $\varphi$  is  
 378 condensed within a narrow range of values). Note that the modeled ODF shown in Fig. 8  
 379 corresponds to the core part of the mesogen that exhibits birefringence at visible wavelengths  
 380 of light.

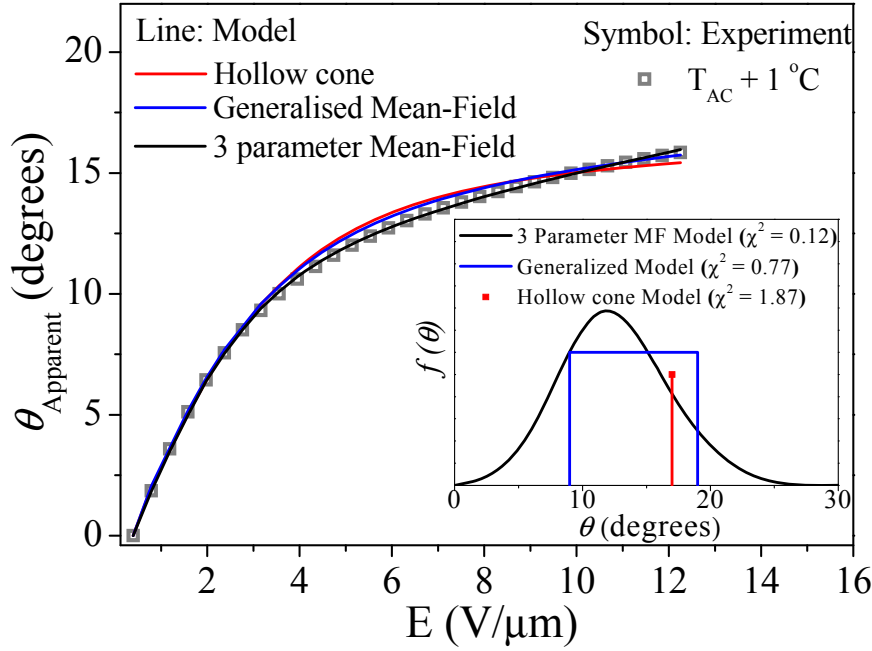


381

382 **FIG. 8.** The ODF of the smectic compound, adpc042, at a temperature of  $T = (T_{AC}$   
 383  $+ 1)$  °C for different electric field strengths (0 V,  $1.3 \text{ V}\mu\text{m}^{-1}$ , and  $12 \text{ V}\mu\text{m}^{-1}$ ). (a-c)  
 384 are the axonometric projections of  $f_{3D}(\theta, \varphi)$ .

385 To test different models, we fit experimental data of  $\theta_{\text{Apparent}}$  as a function of the electric field  
 386 at a temperature 1 °C above the SmA\*- SmC\* phase transition temperature,  $T_{AC}$  (Fig. 9), to  
 387 the following models: the fixed-angle hollow cone [27], the generalized mean-field model  
 388 [28] and our 3-parameter mean-field model. For low fields data fitted to the various models is  
 389 quite adequate. However for the medium and high electric fields, the 3-parameter model  
 390 shows a closer fit to the experimental data. This is supported by drawing a comparison  
 391 between sum of the squares of the residuals ( $\chi^2$ ) for the various fits as shown in the inset of  
 392 Fig. 9. Though, the three models provide reasonable fit to the data, our proposed model has no  
 393 intrinsic assumption of either the sugar-loaf or the diffuse cone type distribution, i.e. it is not  
 394 limited to the assumption of a certain ODF in the SmA\* phase. Therefore testing and  
 395 discrimination among the models is carried out automatically during the fitting procedure.  
 396 Moreover, the model produces a continuous function for the ODF, having a better physical  
 397 significance.

398



399

400 **FIG. 9.** The experimental,  $\theta_{\text{Apparent}}$  ( $\square$ ) vs electric field  $E$  shown at a temperature of 1  
 401  $^{\circ}\text{C}$  above the  $\text{SmA}^*$ -  $\text{SmC}^*$  phase transition temperature,  $T_{\text{AC}}$ , are fitted to various  
 402 models: The hollow cone, the generalized mean Field (MF) and the 3 parameter MF  
 403 one. A schematic representation of the ODFs for the corresponding three models is  
 404 given in the inset.

405 The de Vries LCs normally exhibit large values of the electro-clinic coefficient  
 406 (denoted by  $e$ ) [19, 32, 33]. The electro-clinic response is recorded for the material adpc042  
 407 in a planar-aligned cell. The experiment is carried out by keeping the smectic layer normal at  
 408 an angle of  $22.5^{\circ}$  with respect to the polarizer. The light intensity  $I$ , transmitted through the  
 409 LC cell, in the absence of the field  $E$  is given by:

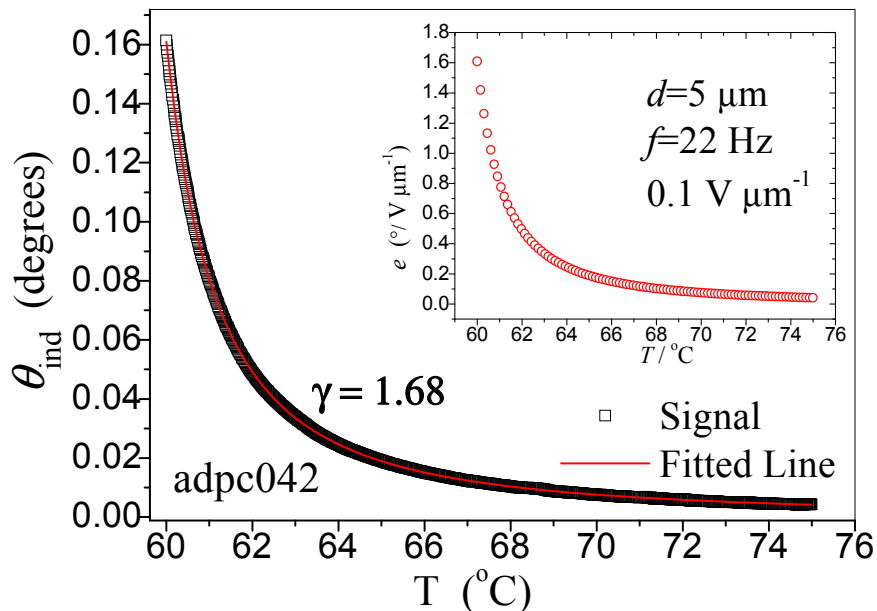
$$410 \quad I = I_0 \sin^2(2\alpha) \sin^2(\pi \Delta n d / \lambda) \quad (6)$$

411  $I_0$  is the incident intensity,  $\alpha$  is the angle between the molecular director and the polarizer,  $\Delta n$   
 412 is the birefringence,  $d$  is the cell thickness, and  $\lambda$  is the wavelength of the incident light.  
 413 When an electric field is applied across the cell, the transmitted intensity varies linearly with  
 414 the induced tilt angle  $\delta\alpha = \theta_{\text{ind}}$ . Differentiating Eq. (6) with respect to  $\alpha$  is given as:

$$415 \quad \delta I = 2I_0 \sin(4\alpha) \sin^2(\pi \Delta n d / \lambda) \theta_{\text{ind}} \quad (7)$$

416 From Eqns. (6) and (7) and for  $\alpha = 22.5^{\circ}$  we obtain  $\theta_{\text{ind}} = \delta I / 4I$ . Figure 10 shows  $\theta_{\text{ind}}$  as a  
 417 function of temperature over the temperature range of  $\text{SmA}^*$  phase. The magnitude of  $\theta_{\text{ind}}$

418 increases with decreasing temperature. On approaching,  $T_{AC}$ , from the high temperature side  
 419 of  $SmA^*$ , magnitude of  $\theta_{ind}$  diverges and this corresponds to the divergence of the correlation  
 420 length of the tilt domain and here the azimuthal angle is condensed to lie within narrower  
 421 limits.



422  
 423 **FIG. 10.** The temperature dependence of electro-clinic response  $\theta_{ind}$  of adpc042 ( $\square$ ):  
 424 experimental value, red line (—): fitting to Eq. (7). The inset figure is the electro-  
 425 clinic co-efficient  $e$  (red open circle  $\square$ ) calculated using the Eq.  $e = \theta_{ind}/E$  as a  
 426 function of temperature. Experiments were conducted under cooling within the  
 427 temperature range of  $SmA^*$  phase up to a temperature of  $T = (T_{AC} + 1) ^\circ C$  by the  
 428 application of  $0.1 V_{0\text{-peak}} \mu m^{-1}$  (planar aligned cell,  $d = 5 \mu m$  sine wave AC voltage of  
 429 22 Hz).

430 The amplitude of  $\theta_{ind}$  with temperature can be expressed by the power law equation as  
 431 follows [34]

$$432 \quad \theta_{ind} = \frac{c}{(T - T_{AC})^\gamma} \quad (8)$$

433 Here  $C$  is the scaling constant,  $T_{AC}$  is the  $SmA^*$ - $SmC^*$  transition temperature and  $\gamma$  is the  
 434 critical exponent. For the smectic material under investigation  $\gamma = 1.68$ . For a conventional  
 435  $SmA^*$ - $SmC^*$  transition,  $\gamma$  is 1.33 [35]. Values of  $\gamma$  greater than 1.33 reflect the short-range  
 436 correlation of molecular directors in three dimensions, again a characteristic of the de Vries  
 437 smectics. The inset plot in Fig. 10 shows the temperature dependence of the electroclinic co-  
 438 efficient  $e$ , calculated from the definition of  $e = \theta_{ind}/E$ .

439

## D. Dielectric Spectroscopy

440

441

442

443

444

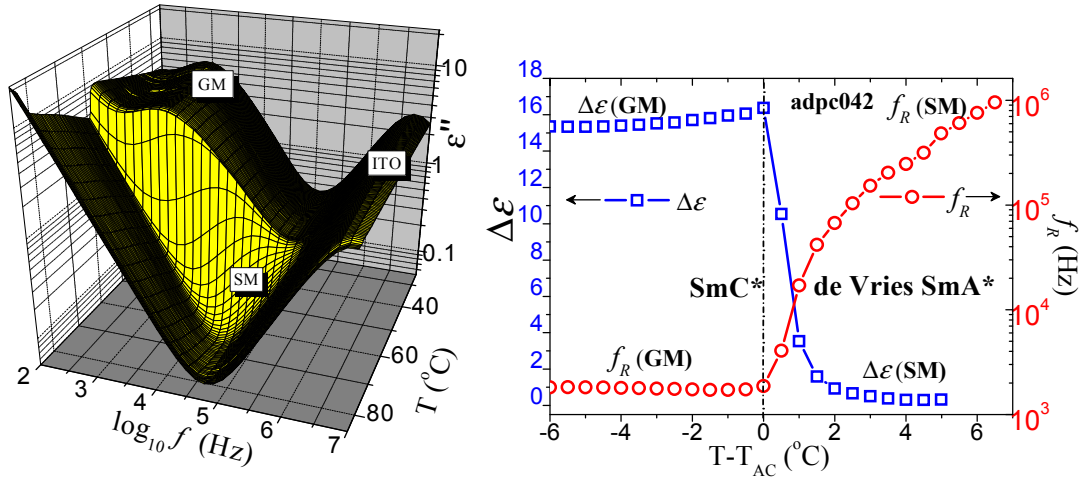
445

446

447

448

Figure 11a shows a three dimensional plot of temperature dependent dielectric loss spectra ( $\varepsilon''$ ) of a planar aligned cell filled with the material adpc042 LC. Note that the temperature independent high frequency process is due to the resistance of ITO in series with the capacitance of the filled cell. The relaxation process in the SmA\* phase corresponds to fluctuation of the tilt angle and this mode is known as the soft mode (SM). This arises mainly as the system approaches  $T_{AC}$  the elastic constant controlling the tilt fluctuations decreases or gets softer. The low frequency dielectric relaxations in the SmC\* phase is associated with the Goldstone (GM) mode in which the molecular director is subjected to continual symmetry breaking.



449

(a)

(b)

450

451

452

453

454

455

456

**FIG. 11.** (a) A 3-D plot of temperature dependent dielectric loss spectra ( $\varepsilon''$ ) of the compound adpc042 (cell thickness,  $d=10 \mu\text{m}$ ) in a planar-aligned cell. The dielectric measurements are carried out under cooling. Temperature stabilization is  $0.05 \text{ }^\circ\text{C}$  and the applied voltage is  $0.1 \text{ V}_{\text{rms}}$  (b) Dielectric strength  $\Delta\varepsilon$  (open blue squares  $\square$ ) and the corresponding relaxation frequency  $f_R$  (red open circles  $\square$ ) as a function of temperature. SM and GM refer to the soft and Goldstone modes, respectively.

457

458

459

The dielectric spectra are analysed using the Novocontrol WINFIT programme. The temperature dependent dielectric strength  $\Delta\varepsilon$  and the relaxation frequency  $f_R$  are obtained by fitting the dielectric spectra to the Havriliak-Negami Eq. [36]:

460

$$\varepsilon^*(\omega) = \varepsilon' - i\varepsilon'' = \varepsilon_\infty + \sum_{j=1}^n \frac{\Delta\varepsilon_j}{[1 + (i\omega\tau_j)^{\alpha_j}]^{\beta_j}} - \frac{i\sigma_{dc}}{\varepsilon_0\omega} \quad (9)$$

461 where,  $\varepsilon_\infty$  is the high frequency permittivity depending on the electronic and atomic  
 462 polarizability,  $j$  is the number of relaxation processes which varies from 1 to  $n$ ,  $\omega=2\pi f$  is the  
 463 angular frequency in radians,  $\varepsilon_0$  is the free space permittivity,  $\tau_j$  is relaxation time of the  $j^{th}$   
 464 process,  $\Delta\varepsilon_j$  is the dielectric strength and  $\alpha_j$  and  $\beta_j$  are the symmetric and asymmetric  
 465 broadening parameters of the  $j^{th}$  dielectric relaxation process related to the distribution of  
 466 relaxation times. The term  $(-i\sigma_{dc}/\varepsilon_0\omega)$  gives the dielectric loss due to the ionic conduction at  
 467 and is dominant at lower frequencies due to the inverse  $\omega$  term. The relaxation frequency  $f_j$  of  
 468 the  $j^{th}$  process is related to  $\tau_j$  as [37]:

$$469 \quad f_j = \frac{1}{2\pi\tau_j} \left[ \sin\left(\frac{\alpha_j\pi}{2+2\beta_j}\right) \right]^{1/\alpha_j} \left[ \sin\left(\frac{\alpha_j\beta_j\pi}{2+2\beta_j}\right) \right]^{-1/\alpha_j} \quad (10)$$

470 The temperature dependencies of  $\Delta\varepsilon$  and  $f_R$  are shown in Fig. 11b. The amplitude of  
 471  $\Delta\varepsilon$  shows a pronounced increase when the system approaches  $T_{AC}$  from the  $SmA^*$  phase. The  
 472 maximum value of  $\Delta\varepsilon$  at  $T_{AC}$  is 16.8. The corresponding  $f_R$  is decreasing in the  $SmA^*$  phase  
 473 with a sharper trend in its lower temperature range. Remarkably strong soft mode dielectric  
 474 absorption is observed in the dielectric spectra of de Vries LCs in contrast to the compounds  
 475 that exhibit a conventional  $SmA^*$  [38-41].

## 476 IV. CONCLUSION

477 We have designed and synthesised two 5-phenyl pyrimidine derivatives with siloxane  
 478 and fluorocarbon chain terminations, both with a chiral (*R,R*)-2,3-epoxyhexoxy side chain.  
 479 Mesophases formed by these compounds are investigated using a number of techniques:  
 480 DSC, POM, XRD, electro-optical, and dielectric spectroscopy.

481 We find that the maximum layer contraction for the siloxane terminated adpc042 at a  
 482 temperature of 13 °C below the  $SmA^*$  -  $SmC^*$  transition is 1.7% and a reduction factor  $R$  is  
 483 0.37 on a scale of 1 to 0. This compound is considered to be a good “de Vries smectic” with  
 484 the de Vries coefficient  $C_{deVries}$  of 0.86 on the scale of 0 to 1. The soft mode dielectric  
 485 relaxation strength  $\Delta\varepsilon$  shows a critical behaviour when the system approaches  $SmA^*$  - $SmC^*$   
 486 transition from the high temperature side. **The critical exponent of the electro-clinic response**  
 487 **is found to be  $\gamma = 1.68$ . Value of the exponent is much greater than 1.33, found for most**  
 488 **conventional smectics. Temperature dependence of the correlation length suggests that the**  
 489 **material has de-Vries characteristics.**

490 We introduce a three parameter MF model for describing the ODF of the molecular  
491 director in SmA\* phase with a view of fitting the field-induced experimental apparent tilt  
492 angle  $\theta_{\text{Apparent}}$  data as a function of the electric field. Close to the SmA\* - SmC\* transition  
493 temperature, the birefringence in SmA\* phase is seen to decrease with a reduction in  
494 temperature. This is due to the emergence of a non-zero value of cone angle  $\theta_0$ , the  
495 magnitude of which increases to  $17^\circ$  as the SmA\*-SmC\* phase transition is approached. The  
496 proposed model fits the experimental data on apparent tilt angle and leads to the diffuse-cone  
497 ODF, at temperatures close to the phase transition temperatures. However  $\theta_0$  decreases with  
498 an increase in temperature and the ODF displays a cross over from the diffuse-cone to the  
499 sugar loaf at  $\sim 3.5^\circ\text{C}$  above  $T_{\text{AC}}$ .

## 500 Acknowledgements

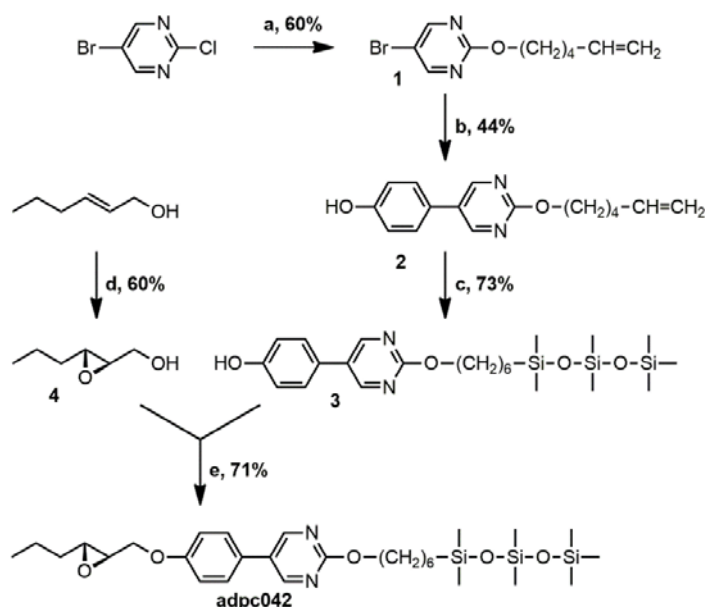
501 Work was supported by 13/US/I2866 from the Science Foundation Ireland as part of the US-  
502 Ireland Research and Development Partnership program jointly administered with the United  
503 States National Science Foundation under grant number NSF-DMR-1410649. Financial  
504 support for the Belfast group was from the Department for Employment and Learning under  
505 with grant code USI 056. X-ray measurements were done in Warsaw, under the EU Cost ICI  
506 1208 2014-17 project. We thank Professor Satyendra Kumar for co-ordinating the US-  
507 Ireland project.

## 508 APPENDIX: SYNTHETIC PROCEDURE

509 All reagents were purchased from Sigma Aldrich, Fluorochem, Alfa Aesar, ABCR,  
510 Synthonix and used without any further purification. Solvents were purchased from Sigma  
511 Aldrich, DMF was purchased pre-dried, THF was dried using a sodium/benzophenone still  
512 under  $\text{N}_2$  and DCM was dried using  $\text{CaH}_2$ . All reactions were generally carried out under  
513 argon using oven-dried glassware. TLC plates were performed on Merck silica gel 60 F<sub>254</sub>  
514 and were visualized using a 254 nm light source. Flash column chromatography was  
515 performed on Fluorochem silica gel 60 (40-63 micron).

516 IR spectra were recorded using a Perkin Elmer Spectrum Two FT-IR spectrometer.  $^1\text{H}$  and  
517  $^{13}\text{C}$  spectra were recorded at  $25^\circ\text{C}$  ( $\text{CDCl}_3$  as solvent and TMS as reference) using a Bruker  
518 400 MHz Ultrashield (Avance 400). HRMS spectra were recorded using a Waters – TOF  
519 Electrospray micromass LCT premier. Optical rotations were recorded using a polarimeter  
520 Perkin Elmer: model 341 Polarimeter.

521 The synthesis of adpc042 was carried out through the scheme shown in FIG. 12.

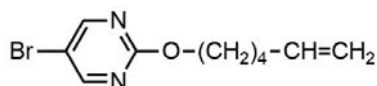


522

523 **FIG. 12.** General scheme for the preparation of **adpc042**

524 Further details of synthesis and characterization of each stage of intermediates are given  
525 below:

526 The chemical structure of compound 1 is given in Fig. 13.



527

528 **FIG. 13.** Chemical structure of compound **1**

529 5-Hexen-1-ol (0.62 g, 6.2 mmol) was dissolved in dry toluene (15 mL) and sealed in a  
530 schlenk under argon. Sodium (0.16 g, 7.00 mmol) was added as a solid and the solution was  
531 stirred at 50 °C overnight. 5-Bromo-2-chloropyrimidine (1.00 g, 5.17 mmol) was added and  
532 the solution stirred for 8 hours at 50 °C. The solution was filtered, water (20 mL) was added  
533 and the crude extracted with ethyl acetate (3 x 30 mL). The product was purified by column  
534 chromatography (ethyl acetate: hexane, 1:9,  $R_f = 0.45$ ) to yield a colourless oil (0.80 g, 3.11  
535 mmol, 60%).

536  $^1\text{H NMR}$  (400 MHz,  $\text{CDCl}_3$ )  $\delta$ : 8.51 (s, 2H), 5.81 (ddt,  $J = 6.67, 6.67, 10.18, 16.91$ , H), 4.98  
537 (m, 2H), 4.33 (t,  $J = 6.60$ , 2H), 2.12 (m, 2H), 1.82 (m, 2H), 1.57 (m, 2H).

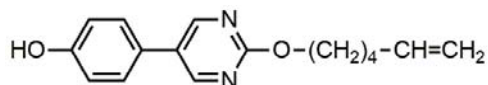


538  $^{13}\text{C}$  NMR (101 MHz,  $\text{CDCl}_3$ )  $\delta$ : 164.15 (C), 159.75 (2CH), 138.59 (CH), 115.01 ( $\text{CH}_2$ ),  
539 111.79 (C), 68.42 ( $\text{CH}_2$ ), 33.55 ( $\text{CH}_2$ ), 28.36 ( $\text{CH}_2$ ), 25.36 ( $\text{CH}_2$ ).

540 IR (film):  $\nu$  = 3076, 2936, 1640, 1570, 1432, 1332, 1176, 1122, 1024, 912, 794  $\text{cm}^{-1}$ .

541 HRMS (EI):  $m/z$  calcd for  $\text{C}_{20}\text{H}_{27}\text{N}_4\text{O}_2\text{Br}_2$  [ $2\text{M} + \text{H}^+$ ] 513.0501, found: 513.0513.

542 The chemical structure of the compound **2** in Fig. 10 is given in Fig. 14 and the synthesis and  
543 characterization are detailed below:



545 **FIG. 14.** Chemical structure of compound **2**

546 4-hydroxyphenylboronic acid (0.32 g, 2.33 mmol) and **1** (0.50 g, 1.94 mmol) were sealed in a  
547 schlenk under argon. Toluene (12 mL) was added and the solution degassed for 5 minutes.  
548 Degassed methanol (7 mL) and potassium carbonate dissolved in degassed water (3 mL)  
549 were added to the schlenk. Tetrakis(triphenylphosphine)palladium(0) (0.11 g, 0.10 mmol)  
550 was added as a solid and the solution was refluxed overnight. The crude was concentrated  
551 and water (30 mL) was added before extraction with DCM (3 x 30 mL). The organic phase  
552 was dried with magnesium sulphate and concentrated in vacuo. The product was purified by  
553 column chromatography (ethyl acetate: DCM, 15:85, where  $R_f$  = 0.57 in ethyl acetate:  
554 hexane, 1:1) to yield a white solid (0.23 g, 0.85 mmol, 44%).

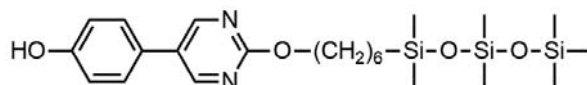
555  $^1\text{H}$  NMR (400 MHz,  $\text{CDCl}_3$ )  $\delta$ : 8.66 (s, 2H), 7.90 (s, 1H), 7.37 (d,  $J$  = 8.72, 2H), 7.03 (d,  $J$  =  
556 8.71), 5.79 (ddt,  $J$  = 6.65, 6.65, 10.18, 16.91, 1H), 4.97 (m, 2H), 4.42 (t,  $J$  = 6.58, 2H), 2.11  
557 (m, 2H), 1.85 (m, 2H), 1.58 (m, 2H).

558  $^{13}\text{C}$  NMR (101 MHz,  $\text{CDCl}_3$ )  $\delta$ : 164.22 (C), 157.17 (C), 156.95 (2CH), 138.61 (CH), 128.48  
559 (C), 127.98 (2CH), 126.19 (C), 116.73 (2CH), 114.97 ( $\text{CH}_2$ ), 68.06 ( $\text{CH}_2$ ), 33.55 ( $\text{CH}_2$ ),  
560 28.48 ( $\text{CH}_2$ ), 25.38 ( $\text{CH}_2$ ).

561 IR (film):  $\nu$  = 3099, 3022, 2950, 1602, 1558, 1434, 1326, 1270, 1180, 1072, 924, 834  $\text{cm}^{-1}$ .

562 HRMS (EI): The molecular weight for  $\text{C}_{16}\text{H}_{19}\text{N}_2\text{O}_2$  [ $\text{M} + \text{H}^+$ ] was calculated as 271.1447  
563 and found to be 271.1446.

564 The chemical structure of compound **3** is given in Fig. 15; synthesis and characterization are  
565 detailed below:



567

**FIG. 15.** Chemical structure of compound **3**

568 **2** (0.22 g, 0.81 mmol) was dissolved in dry THF (12 mL) under argon. 1,1,1,3,3,5,5-  
569 heptamethyltrisiloxane (0.35 g, 1.59 mmol) and platinum(0)-1,3-divinyl-1,1,3,3-  
570 tetramethyldisiloxane (0.20 mL of 0.1M solution, 0.02 mmol) were added to the flask and the  
571 solution was stirred for 2 hours. The crude is concentrated and purified by column  
572 chromatography (ethyl acetate: hexane, 2:8, where  $R_f = 0.30$  in ethyl acetate: hexane, 3:7) to  
573 yield a colourless wax (0.29 g, 0.59 mmol, 73%).

574  **$^1\text{H}$  NMR (400 MHz,  $\text{CDCl}_3$ )  $\delta$ :** 8.65 (s, 2H), 7.39 (d,  $J = 8.70$ ), 6.96 (d,  $J = 8.72$ , 2H), 5.37  
575 (s, 1H), 4.39 (t,  $J = 6.72$ ), 1.83 (m, 2H), 1.42 (m, 6H), 0.54 (m, 2H), 0.08 (s, 9H), 0.06 (s,  
576 6H.), 0.02 (s, 6H).

577  **$^{13}\text{C}$  NMR (101 MHz,  $\text{CDCl}_3$ )  $\delta$ :** 164.71 (C), 157.08 (CH), 156.18 (C), 128.11 (CH), 128.08  
578 (C) 127.30 (C), 116.48 (CH), 68.19 ( $\text{CH}_2$ ), 33.36 ( $\text{CH}_2$ ), 29.07 ( $\text{CH}_2$ ), 25.91 ( $\text{CH}_2$ ), 23.39  
579 ( $\text{CH}_2$ ), 18.47 ( $\text{CH}_2$ ), 2.04 (3 $\text{CH}_3$ ), 1.50 (2 $\text{CH}_3$ ), 0.41 (3 $\text{CH}_3$ ).

580 **IR (film):**  $\square = 2958, 1600, 1442, 1332, 1258, 1048, 840 \text{ cm}^{-1}$ .

581 **HRMS (EI):**  $m/z$  calcd for  $\text{C}_{23}\text{H}_{41}\text{N}_2\text{O}_4\text{Si}_3$  [ $\text{M} + \text{H}^+$ ] 493.2374, found: 493.2379.

582 The chemical structure of compound **4** is given in Figure **16** and other details are followed  
583 below:



584

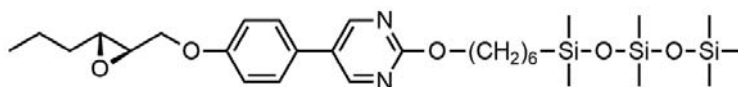
585

**FIG. 16.** Chemical structure of compound **4**

586 Trans-2-hexen-1-ol (1.00 g, 9.98 mmol), Shi Epoxidation Diketal Catalyst (0.77 g, 3.00  
587 mmol) and Tetrabutylammonium hydrogensulfate (0.06 g, 0.18 mmol) were dissolved in  
588 dimethoxymethane/acetonitrile (100 mL, 2:1). Acetic acid (0.35 mL) was added to potassium  
589 carbonate (70 mL of 0.1M solution) and this was added to the reaction which was then cooled  
590 to  $-10 \text{ }^\circ\text{C}$ . Oxone (8.48 g, 13.78 mmol) was dissolved in ethylenediaminetetraacetic acid  
591 disodium salt (50 mL of 0.004M solution in water) and potassium carbonate (8.00 g, 57.91  
592 mmol) was dissolved in water (50mL). The oxone and the carbonate solution were added to  
593 the reaction flask dropwise over 3 hours while keeping the temperature below  $0 \text{ }^\circ\text{C}$ . Water  
594 was added and the organic phase extracted with DCM (3 x 50 mL) before drying with  
595 magnesium sulphate and concentrating the solution. The epoxide was purified by column  
596 chromatography (hexane: diethyl ether, 2:1  $\rightarrow$  100% ether once product appears,  $R_f = 0.53$  in

597 DCM: ethyl acetate, 1:1) to yield a colourless oil (0.70 g, 5.99 mmol, 60%). The column was  
598 compacted using hexane: diethyl ether, 2:1 and 1% triethylamine to neutralize the silica.  
599  $^1\text{H NMR}$  (400 MHz,  $\text{CDCl}_3$ )  $\delta$ : 3.91 (ddd,  $J = 2.58, 5.58, 12.53$ , 1H), 3.63 (ddd,  $J = 4.30$ ,  
600 7.29, 12.52), 2.96 (td,  $J = 2.36, 5.50, 5.65$ , 1H), 2.92 (m, 1H), 1.74 (m), 1.50 (m, 3H), 0.96 (t,  
601  $J = 7.26$ , 3H).  
602  $^{13}\text{C NMR}$  (101 MHz,  $\text{CDCl}_3$ )  $\delta$ : 61.93 ( $\text{CH}_2$ ), 58.55 (CH), 56.01 (CH), 33.78 ( $\text{CH}_2$ ), 19.47  
603 ( $\text{CH}_2$ ), 14.10 ( $\text{CH}_3$ ).  
604 **IR (film)**:  $\square = 3418, 2962, 2874, 1650, 1464, 1382, 1220, 1046, 900, 849 \text{ cm}^{-1}$ .  
605  $[\alpha]_{\text{D}}^{20}$ : +38.75 (c 0.022,  $\text{CHCl}_3$ ).

606 The chemical structure of adpc042 is given in Fig. 17 and other details are followed below:



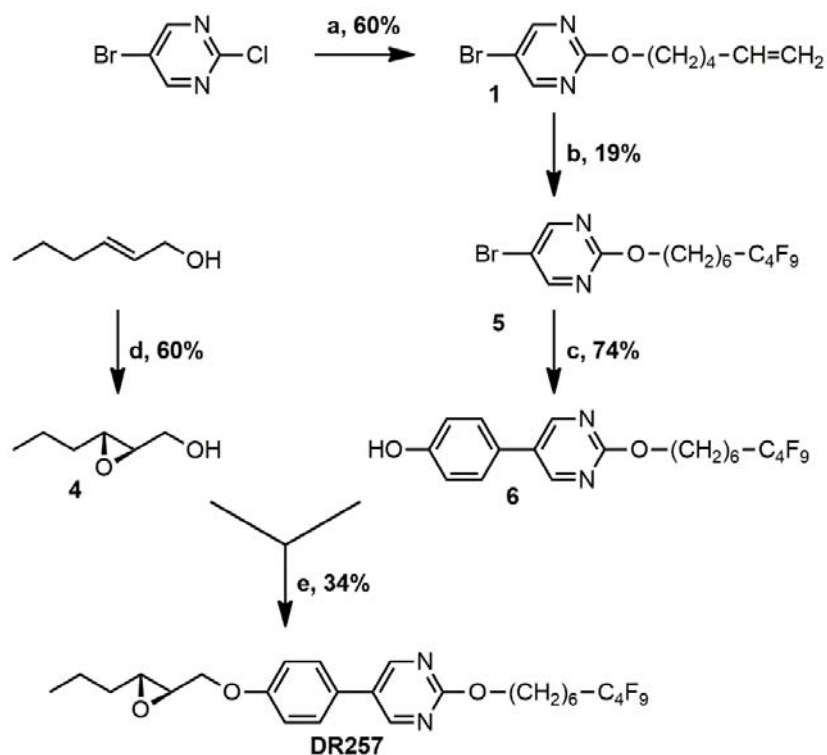
607

608

**FIG. 17.** Chemical structure of compound **adpc042**

609 **3** (0.56 g, 1.14 mmol), **4** (0.12 g, 1.03 mmol) and triphenylphosphine (0.33 g, 1.26 mmol)  
610 were dissolved in dry THF (20 mL) under argon. Diethyl azodicarboxylate (0.22 g, 1.24  
611 mmol) was dissolved in dry THF (8 mL) under argon before being added dropwise to the  
612 reaction flask. The flask was stirred overnight and then concentrated. The product was  
613 purified by column chromatography (ethyl acetate: hexane, 1:9, where  $R_f = 0.60$  in ethyl  
614 acetate: hexane, 3:7) to yield a white wax (0.43 g, 0.73 mmol, 71%).  
615  $^1\text{H NMR}$  (400 MHz,  $\text{CDCl}_3$ )  $\delta$ : 8.65 (s, 2H), 7.43 (d,  $J = 8.81$ , 2H), 7.02 (d,  $J = 8.81$ , 2H),  
616 4.38 (t,  $J = 6.71$ , 2H), 4.23 (dd,  $J = 3.34, 11.08$ , 1H), 4.02 (dd,  $J = 5.52, 11.08$ ), 3.13 (ddd,  $J =$   
617 2.29, 3.27, 5.53, 1H), 2.98 (td,  $J = 2.20, 5.53, 5.64$ , 1H), 1.83 (m, 2H), 1.65-1.30 (m, 10H),  
618 0.99 (t,  $J = 7.28$ ), 0.54 (m, 2H), 0.08 (s, 9H), 0.06 (s, 6H), 0.01 (s, 6H).  
619  $^{13}\text{C NMR}$  (101 MHz,  $\text{CDCl}_3$ )  $\delta$ : 164.76 (C), 158.92 (C), 157.10 (2CH), 127.95 (C), 127.89  
620 (2CH), 127.68 (C), 115.71 (2CH), 68.82 ( $\text{CH}_2$ ), 68.15 ( $\text{CH}_2$ ), 56.66 (CH), 56.22 (CH), 33.84  
621 ( $\text{CH}_2$ ), 33.36 ( $\text{CH}_2$ ), 29.06 ( $\text{CH}_2$ ), 25.91 ( $\text{CH}_2$ ), 23.39 ( $\text{CH}_2$ ), 19.44 ( $\text{CH}_2$ ), 18.46 ( $\text{CH}_2$ ), 14.10  
622 ( $\text{CH}_3$ ), 2.04 (3 $\text{CH}_3$ ), 1.50 (2 $\text{CH}_3$ ), 0.40 (2 $\text{CH}_3$ ).  
623 **IR (film)**:  $\square = 2958, 1598, 1548, 1448, 1256, 1048, 840 \text{ cm}^{-1}$ .  
624 **HRMS (EI)**:  $m/z$  calcd for  $\text{C}_{29}\text{H}_{51}\text{N}_2\text{O}_5\text{Si}_3$  [ $\text{M} + \text{H}^+$ ] 591.3096, found: 591.3097.  
625  $[\alpha]_{\text{D}}^{20}$ : +9.74 (c 0.029,  $\text{CHCl}_3$ ).

626 The synthesis of DR257 was carried out through the scheme shown in FIG. 18, further details  
627 of each stage are provided below.

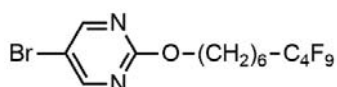


628

629

**FIG. 18.** General scheme for the preparation of **DR257**

630 Synthesis and characterization of the intermediates are given below. Structure of the  
631 compound 5 is given in Fig. 19 and details follow below:



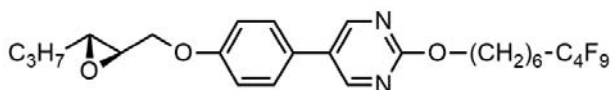
632

633

**FIG. 19.** The Chemical structure of compound 5

634  $\text{Na}_2\text{S}_2\text{O}_4$  (0.040 g, 0.230 mmol) and  $\text{Na}_2\text{HPO}_4$  (0.039 g, 0.276 mmol) were added to a  
635 mixture of 1-iodoperfluorobutane (0.955 g, 2.76 mmol), the alkene 1 (0.590 g, 2.30 mmol) in  
636  $\text{H}_2\text{O}/\text{CH}_3\text{CN}$  (12 mL 1:3) [42]. The mixture was stirred overnight at room temperature.  $\text{Et}_2\text{O}$   
637 and  $\text{H}_2\text{O}$  were added to the mixture and the phases were separated. The organic phase was  
638 extracted with  $\text{Et}_2\text{O}$  (2 X 10 mL) and the combined organic phase was dried with magnesium  
639 sulphate. The solvent was removed at reduce pressure to led a yellow oil. This iodinated  
640 intermediate was used without further purification.  $\text{Bu}_3\text{SnH}$  (0.802 g, 2.76 mmol) and a  
641 catalytic amount of AIBN (12 mg) were added to the oil. The reaction mixture was heated to





673

674

**FIG. 21.** Chemical structure of compound **DR257**

675 **6** (0.220 g, 0.449 mmol), **4** (0.048 g, 1.03 mmol) and triphenylphosphine (0.129 g, 0.490  
 676 mmol) were dissolved in dry THF (10 mL) under argon. Diethyl azodicarboxylate (0.085 g,  
 677 0.490 mmol) was dissolved in dry THF (4 mL) under argon before being added dropwise to  
 678 the reaction flask. The flask was stirred overnight and then concentrated. The product was  
 679 purified by column chromatography (ethyl acetate: hexane, 1.5:9, where  $R_f = 0.60$  in ethyl  
 680 acetate: hexane, 3:7) to yield a white powder (0.82 g, 0.140 mmol, 34%).

681  **$^1\text{H}$  NMR (400 MHz,  $\text{CDCl}_3$ )  $\delta$ :** 8.65 (s, 2H), 7.42 (m, 2H), 7.01 (m, 2H), 4.39 (t,  $J = 6.5$ ,  
 682 2H), 4.23 (dd,  $J = 11.1, 3.3$ , 1H), 4.01 (dd,  $J = 11.1, 5.5$ , 1H), 3.12 (m, 1H), 2.97 (m, 1H),  
 683 2.06 (m, 2H), 1.90 – 1.80 (m, 2H), 1.69 – 1.40 (m, 10H), 0.98 (t,  $J = 7.3$ , 3H).

684  **$^{13}\text{C}$  NMR (101 MHz,  $\text{CDCl}_3$ )  $\delta$ :** 164.63 (C), 158.94 (C), 157.09 (2CH), 128.08 (C), 127.87  
 685 (2CH), 127.56 (C), 115.70 (2CH), 68.81 ( $\text{CH}_2$ ), 67.72 ( $\text{CH}_2$ ), 56.61 (CH), 56.20 (CH), 33.81  
 686 ( $\text{CH}_2$ ), 30.91 (t,  $J = 22.3$ ,  $\text{CH}_2$ ), 29.02 ( $\text{CH}_2$ ), 28.84 ( $\text{CH}_2$ ), 25.88 ( $\text{CH}_2$ ), 20.25 (t,  $J = 3.7$ ,  
 687  $\text{CH}_2$ ), 19.41 ( $\text{CH}_2$ ), 14.06 ( $\text{CH}_3$ ).

688  **$^{19}\text{F}$  NMR (376 MHz,  $\text{CDCl}_3$ )  $\delta$ :** -81.08, -114.63, -124.52, -126.08.

689 **HRMS (EI):**  $m/z$  calcd for  $\text{C}_{26}\text{H}_{30}\text{F}_9\text{N}_2\text{O}_3$  [ $\text{M} + \text{H}^+$ ] 589.2097, found 589.2104.

690  **$[\alpha]_D^{20}$ :** +8.868 (c 0.0106,  $\text{CHCl}_3$ ).

## 691 **References:**

692 [1] N. A. Clark and S. T. Lagerwall, *Appl. Phys. Lett.* **36**, 899 (1980).

693 [2] S. T. Lagerwall, *Ferroelectric and Antiferroelectric Liquid Crystals*, Wiley-VCH,  
 694 Weinheim (1999).

695 [3] T. P. Rieker, N. A. Clark, G. S. Smith, D. S. Parmar, E. B. Sirota and C. R. Safinya, *Phys.*  
 696 *Rev. Lett.* **59**, 2658 (1987).

697 [4] J. P. Lagerwall and F. Giesselmann, *Chem. Phys. Chem.* **7**, 20 (2006).

698 [5] M. V. Gorkunov, F. Giesselmann, J. P. F. Lagerwall, T. J. Sluckin and M. A. Osipov,  
 699 *Phys. Rev. E* **75**, 060701 (2007).

700 [6] M. V. Gorkunov, M. A. Osipov, J. P. F. Lagerwall and F. Giesselmann, *Phys. Rev. E* **76**,  
 701 051706 (2007).

702 [7] K. Saunders, D. Hernandez, S. Pearson and J. Toner, *Phys. Rev. Lett.* **98**, 197801 (2007).

- 703 [8] K. Saunders, Phys. Rev. E **77**, 061708 (2008).
- 704 [9] V. Swaminathan, V. P. Panov, Yu. P. Panarin, S. P. Sreenilayam, J. K. Vij, A. Panov, D.  
705 Rodriguez-Lojo, P. J. Stevenson, and E. Gorecka, Liq. Cryst., <https://doi.org/10.1080/02678292.2017.1359694> (2017).  
706
- 707 [10] H. G. Yoon, D. M. Agra-Kooijman, K. Ayub, R. P. Lemieux, and S. Kumar, Phys. Rev.  
708 Letts., **106**, 087801(2011); D. M. Agra-Kooijman, H. G. Yoon, S. Dey, and S. Kumar,  
709 Phys. Rev. E **89**, 032506 (2014).
- 710 [11] Y. Gao, J. M. Klunder, R. M. Hanson, H. Masamune, S. Y. Ko, and K. B. Sharpless, J.  
711 Am. Chem. Soc. **109**, 5765 (1987); Y. Tu, Z. Wang, and Y. Shi, J. Am. Chem. Soc. **118**,  
712 9806 (1996).
- 713 [12] D. Nonnenmacher, M. A. Osipov, J. C. Roberts, R. P. Lemieux, and F. Giesselmann,  
714 Phy. Rev. E **82**, 031703 (2010).
- 715 [13] C. P. J. Schubert, C. Muller, F. Giesselmann, and R. P. Lemieux, J. Mater. Chem. C **4**,  
716 8483 (2016).
- 717 [14] J. C. Roberts, N. Kapernaum, Q. Song, D. Nonnenmacher, K. Ayub, F. Giesselmann,  
718 and R. P. Lemieux, J. Am. Chem. Soc. **132**, 364 (2010).
- 719 [15] C. P. J. Schubert, A. Bogner, J. H. Porada, K. Ayub, T. Andrea, F. Giesselmann, and R.  
720 P. Lemieux, J. Mater. Chem. C **2**, 4581 (2014).
- 721 [16] A. de Vries, J. Chem. Phys. **71**, 25 (1979).
- 722 [17] G. W. Gray and J. W. Goodby, *Smectic Liquid Crystals*, Leonard Hill, London (1984).
- 723 [18] A. de Vries, Mol. Cryst. Liq. Cryst. **41**, 27 (1977).
- 724 [19] J. W. Goodby, Ch. 3, *Handbook of Liquid Crystals*, Volume 1, 2nd ed., Wiley-VCH  
725 (2015) [editors: J. W. Goodby, P. J. Collings, T. Kato, C. Tschierske, H. F. Gleeson, P.  
726 Raynes]
- 727 [20] J. Naciri, G. P. Crawford, B. R. Ratna, and R. Shashidhar, Ferroelectrics **148**, 297  
728 (1993).
- 729 [21] Y. Takanishi, Y. Ouchi, H. Takezoe, A. Fukuda, A. Mochizuki, and M. Nakatsuka, Jpn.  
730 J. Appl. Phys. **29**, L984 (1990).
- 731 [22] L. Li, C. D. Jones, J. Magolan, and R. P. Lemieux, J. Mater. Chem. **17**, 2313 (2007).
- 732 [23] B. Park, S. -S. Seomun, M. Nakata, and M. Takahashi, Jpn. J. Appl. Phys. **38**, 1474  
733 (1999).
- 734 [24] V. M. Vaksman and Yu. P. Panarin, Mol. Mater. **1**, 147 (1992); V. Panov, J. K. Vij, and  
735 N. M. Shtykov, Liq. Cryst. **28**, 615 (2001).
- 736 [25] S. Inui, N. Iimura, T. Suzuki, H. Iwane, K. Miyachi, Y. Takanishi, and A. Fukuda, J.  
737 Mater. Chem. **6**, 671 (1996).
- 738 [26] S. Garoff and R. B. Meyer, Phys. Rev. Lett. **38**, 848 (1977).

- 739 [27] N. A. Clark, T. Bellini, R.-F. Shao, D. Coleman, S. Bardon, D. R. Link, J. E. MacLennan,  
740 X.-H. Chen, M. D. Wand, D. M. Walba, P. Rudquist, and S. T. Lagerwall, *Appl. Phys.*  
741 *Lett.* **80**, 4097 (2002).
- 742 [28] Y. Shen, L. Wang, R. Shao, T. Gong, C. Zhu, H. Yang, J. E. MacLennan, D. M. Walba,  
743 and N. A. Clark, *Phys. Rev. E* **88**, 062504 (2013).
- 744 [29] S. T. Lagerwall, P. Rudquist, and F. Giesselmann, *Mol. Cryst. Liq. Cryst.* **510**, 148  
745 (2009).
- 746 [30] J. V. Selinger, P. J. Collings, and R. Shashidhar, *Phys. Rev. E* **64**, 061705 (2001).
- 747 [31] R. Qiu, J. T. Ho, and S. K. Hark, *Phys. Rev. A* **38**, 1653 (1988).
- 748 [32] F. Giesselmann, P. Zugenmaier, I. Dierking, S. T. Lagerwall, B. Stebler, M. Kaspar, V.  
749 Hamplova, and M. Glogarova, *Phys. Rev. E* **60**, 598 (1999).
- 750 [33] O. E. Panarina, Yu. P. Panarin, J. K. Vij, M. S. Spector, and R. Shashidhar, *Phys. Rev. E*  
751 **67**, 051709 (2003).
- 752 [34] K. L. Sandhya, Yu. P. Panarin, V. P. Panov, J. K. Vij, and R. Dabrowski, *Eur. Phys. J. E*  
753 **27**, 397 (2008).
- 754 [35] P. G. de Gennes and J. Prost, *The Physics of Liquid Crystals*, Clarendon, Oxford (1993).
- 755 [36] S. Havriliak (Jr.) and S. Negami, *Polymer* **8**, 161 (1967).
- 756 [37]. O. E. Kalinovskaya and J. K. Vij, *J. Chem. Phys.* **111**, 10979 (1999).
- 757 [38] H. Xu, J. K. Vij, A. Rappaport, and N. A. Clark, *Phys. Rev. Lett.* **79**, 249 (1997).
- 758 [39] U. Manna, J. -K. Song, Yu. P. Panarin, A. Fukuda, and J. K. Vij, *Phys. Rev. E* **77**,  
759 04170 (2008).
- 760 [40] S. P. Sreenilayam, D. M. Agra-Kooijman, V. P. Panov, V. Swaminathan, J. K. Vij, Yu.  
761 P. Panarin, A. Kocot, A. Panov, D. Rodriguez-Lojo, P. J. Stevenson, M. R. Fisch, and S.  
762 Kumar, *Phys. Rev. E* **95**, 032701 (2017).
- 763 [41] N. Yadav, V. P. Panov, V. Swaminathan, S. P. Sreenilayam, J. K. Vij, T. S. Perova, R.  
764 Dhar, A. Panov, D. Rodriguez-Lojo, and P. J. Stevenson, *Phys. Rev. E* **95**, 062704 (2017).
- 765 [42] J. Q. Huang, W. D. Meng, and F. L. Qing *J. Fluor. Chem.* **128**, 1469 (2007).